

Emergence of Collective Behaviors from Local Voronoi Topological Perception

Ivan Gonzalez*, Jack Tisdell†, Rustum Choksi‡, and Jean-Christophe Nave§

Department of Mathematics and Statistics, McGill University

September 21, 2023

Abstract

This article addresses the emergence of collective agent behaviors from simple and realistic decisions made at the level of the local Voronoi diagram, i.e., the Voronoi region (*personal space*) of agents and their neighboring agents in the sense of the Voronoi diagram. We present a discrete time model in 2D in which individual agents are aware of their local Voronoi environment and may seek static target locations. Our deterministic model incorporates features common to many other “active matter” models like collision avoidance, alignment among agents, and homing toward targets. However, it is novel in key respects: the model combines topological and metrical features in a natural manner based upon the agents local perception of their Voronoi cell. With at most two control parameters, it is shown numerically to capture a wide range of collective behaviors. It is also shown that the Voronoi topology facilitates the computation of several novel observables for quantifying discrete collective behaviors.

1 Introduction

The connection between individual and collective behavior in biological systems has fascinated researchers for decades. A well-studied paradigm entails the tendency of groups of individual agents to form flocks, swarms, herds, schools, etc. As we discuss further in Section 2, many mathematical models from discrete to continuum have been presented and studied to capture the emergence of collective behaviors from postulated local laws. These models comprise components—for example, averaging orientation directions over Euclidean distances to favor alignment or phenomenological interaction potentials (kernels) for repulsion/attraction—which in addition to facilitating numerical computations, lend themselves well to formal, rigorous, or multiscale mathematical analysis.

Here we take a different approach, divorced from any underlying goal/bias for the potential mathematical analysis of the model. We directly address what we believe to be an important and useful question in the modelling of collective behavior: how do collective behaviors emerge from simple and realistic decisions made at the level of local Voronoi diagram? More specifically, suppose we consider a finite set of agents, characterized by points in some domain. We view an agent’s Voronoi cell as its *personal space* and employ the following hypotheses:

Repulsion There exists an intrinsic length scale L associated with the agents (the *repulsive falloff distance*) below which an agent favors repulsion away from its closest (Voronoi) neighbouring agent.

Homing All or some of the agents have a tendency to seek targets.

Alignment Agents have a tendency to align (weighted with a dimensionless parameter ν) their directional movement with those of (Voronoi) neighbouring agents, favoring those with relatively similar directions.

Personal Space Speed Adjustment Once a movement direction is set via a suitable combination of the previous three components, the agents adjust their speed based upon their personal space (Voronoi cell) via **either** the area of their *visible* personal space (Model I) or the length of their *personal geodesic* (Model II), See Fig. 3 for a quick schematic and Section 3.1.5 for a precise definition.

We believe the Voronoi topology is natural for agent perception and moreover, facilitates an *effective synthesis* of these three competing components. This synthesis results in a simple model prescribing the discrete time agent evolution which we call Voronoi Topological Perception (VTP). The VTP model:

- (i) is based entirely on realistic and cognitively cheap decisions of the agents local perception in the Voronoi topology;
- (ii) via the computation of the Delaunay triangularization, is computationally simple (particularly so in 2D);

*ivan.gonzalez@mail.mcgill.ca

†jack.tisdell@mail.mcgill.ca

‡rustum.choksi@mcgill.ca

§jean-christophe.nave@mcgill.ca

- (iii) with at most two controlling parameters, leads to the emergence of a wide class of collective behaviors predicted by well-established models (with or without stochastic components) and, to our knowledge, leads to collective behaviours which have not been previously predicted;
- (iv) is amenable to generalization like the inclusion of sources, sinks, obstacles, aggregation, and the ability to model different agent behaviors (heterogeneous crowds).

Let us first highlight the drawback for working in this discrete Voronoi topology: the rigid nonlocal framework of the Voronoi diagram (with topological changes at each time step) results in a model which is extremely difficult to analyze (even formally) in any precise mathematical framework. Indeed, the interesting collective behaviors are not in asymptotic parameter regimes and mean field (continuum) limits are intractable. While we certainly acknowledge this as a weakness from a modelling point of view, we nevertheless feel the merits of our motivation, its simple deterministic structure, its computational efficiency, and its numerical predictions warrant the presentation here. Henceforth our analysis of the VTP method is purely numerical; however we stress that an additional advantage of the Voronoi setting is that it facilitates the computation of several observables to quantify certain generic collective behaviors. As we describe in Sections 4.1 and 5, these include Voronoi-based notions of *clustering, pressure, percolation, and queuing*. To our knowledge, these observables are new in the large collective behavior literature, and can be applied not just to our VTP model but to *any* discrete agent-based model.

Our goal here is not to exhaust the possibilities of VTP nor tailor it to a specific biological or engineering system. Rather we focus on two canonical scenarios: a point target and the bi-directional hallway. For the former, we work on the infinite plane and demonstrate interesting behaviors, including a novel *breathing* regime seen only with Model I. For the later, we consider a bi-directional hallway cast as an elongated rectangular domain (with repelling horizontal walls). Each of the narrow edges acts as a source where, at each iteration, agents appear according to a (state-dependent) probability distribution defined on that edge. Agents generated at the left target the right wall and vice-versa. In addition to L and ν , one additional control parameter L_s is related to the source probability distribution. Here we explore lane formation and occlusion/percolation.

In order to appreciate the VTP model, we supplement the article with a Github site¹. Here one finds dynamic simulations for the runs discussed here and many more. For example, one can view simulations (run in real time) of single and multiple point targets as well higher-dimensional targets on an infinite domain for both Model I and II. One can also adjust parameters during the course

of the simulation. We also include some sample simulations for the bi-directional hallway with Model I, illustrating the six regimes eluded to in Section 5. Lastly, we include sample simulations for collective behaviors on compact manifolds without boundary (the flat torus and the 2-sphere). Note that for all simulations, one can download the code for further experimentation with VTP.

1.1 Outline of the Two VTP Models

We briefly summarize the VTP model, with reference to Section 3 for details. To the i -th agent we associate a position vector $x_i(t)$ at time $t = 0, 1, 2, \dots$. Note that time here is arbitrary, and hence the discrete time step is set to unity. Our model views the Voronoi diagram associated with the agent positions as fundamental to their perception (see Fig. 1).

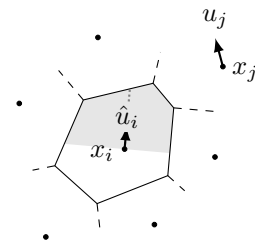
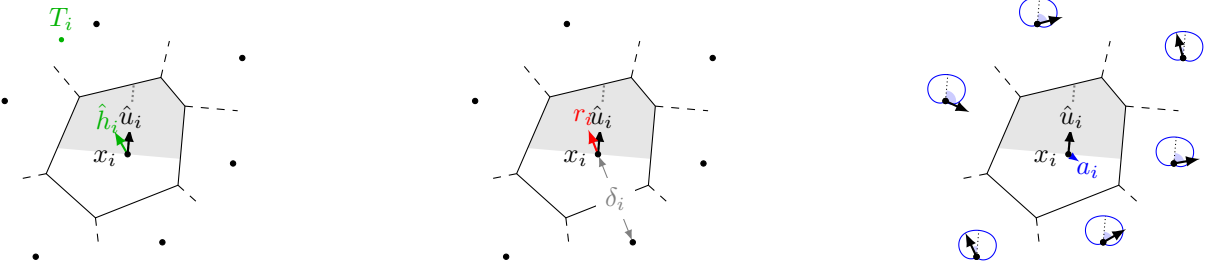


Figure 1: At each time t , the i -th agent located at x_i , its “orientation” vector \hat{u}_i , and its Voronoi-neighboring agents (the position of a generic neighbor is labelled as x_j). Its personal space (Voronoi cell) is depicted with the visible part shaded.

At each time step t , we associate to the i -th agent its **displacement vector** $u_i(t) := x_i(t) - x_i(t-1)$. We denote by $\hat{u}_i(t)$ the unit vector in the direction $u_i(t)$ and refer to it as the i -th agent **orientation (or direction) vector** at time t . Since the time step is set to unity, we associate the magnitude of $u_i(t)$ with the i -th agent **speed** at time t . After a given initial position and orientation selection, the trajectory is prescribed by a rule relating $u_i(t+1)$ to the positions and orientations vectors of the Voronoi-neighboring agents at the previous time step t . The rule (cf. (1) and (2)) encapsulates (or synthesizes) the three components via the following steps. **Note:** In the sequel, we usually suppress the explicit dependence of state variables on t .

The Repulsion Plus Homing Component: When the closest Voronoi-neighbor is within a distance L , a repulsive component pushes the i -th agent x_i away from its closest neighbour (cf. (3)). This short-range repulsion mechanism is dubbed MACN (moving away from the closest neighbor) and captures a cognitively cheap representation of repulsion. While it does introduce short time/short distance sporadic oscillations due to changes in the Voronoi topology, these are all filtered out over

¹<https://jacktisdell.github.io/Voronoi-Topological-Perception>



(a) **Homing.** Unit homing vector \hat{h}_i points toward target T_i , if it is nonempty and does not contain x_i . (Here the target is shown as a dot but may be any region, in general.)

(b) **Repulsion.** Repulsion vector r_i always points away from nearest neighbor or domain boundary. The distance δ_i to this nearest neighbor determines the relative weight of r_i and \hat{h}_i .

(c) **Alignment.** Alignment a_i is given by a weighted average of the velocities of Voronoi neighbors. The circularly-wrapped weighting functions are indicated by the blue curves where the relative angle marked with light blue sectors is the argument.

Figure 2: **Schematic of the influences** on a generic agent at time t . Here we show one agent i at position x_i as well as its Voronoi cell and Voronoi neighbors whose positions are marked with black dots. We illustrate the three components which influence i 's motion in the triptych above. Repulsion r_i and homing \hat{h}_i are weighted with coefficients $\sigma(\delta_i/L)$ and convex compliment $1 - \sigma(\delta_i/L)$, respectively, where δ_i is the distance to i 's nearest neighbor, as shown in (a) above. The relative weight of alignment a_i is given by the parameter ν . We also show shaded in light gray, the region within i 's Voronoi cell in front of i whose area (appropriately nondimensionalized) contributes to i 's next step size.

longer distances. We label the unit repulsive direction of the i -th agent by r_i .

Simultaneously, the agent may have a homing unit direction vector towards its closest target, labelled h_i (cf. (6)). A convex combination with weight $0 \leq \sigma_i \leq 1$ of these two directions is taken which favours repulsion the closer the nearest neighboring agent is (cf. (7)). The weight σ_i depends on the ratio of the distance δ_i from agent i to its closest Voronoi-neighbor and L . When $\delta_i/L \geq 1$ (well separated), there is no repulsion and homing is given full weight. Note that this combined repulsion/homing component $\sigma_i r_i + (1 - \sigma_i) h_i$ is controlled via the parameter L .

The Alignment Component: Like the much-studied model of Vicsek et. al. [46], the later introduced model by Cucker and Smale [12], as well as their numerous posterior extensions, the primary organizational mechanism in our model is the alignment component of each agent. However, as opposed to these other models, our averaging scheme for this primary component does not depend on the metric distance between the agents but rather on the relative directional differences with Voronoi-neighboring agents. To this end, equations (4) and (5) present the alignment directional component a_i as a weighted average of the directions \hat{u}_j of the Voronoi-neighbours. The relative strength of the alignment component a_i is controlled via a multiplicative dimensionless factor ν .

Normalization and Speed Adjustment to Determine $u_i(t+1)$: The sum of the repulsion/homing component with the alignment component $\sigma_i r_i + (1 - \sigma_i) h_i + \nu a_i$

gives the direction for $u_i(t+1)$. To determine its mag-

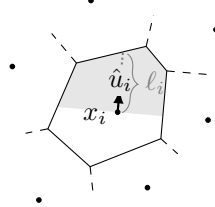


Figure 3: Speed determined by two different geometric perceptions of the personal space: visible area (the shaded region) or length ℓ_i of the leading geodesic.

nitude (the step size), we (approximately) normalize the sum and then rescale based upon either **Model I:** the **scaled area** of the agent's *visible* Voronoi cell depicted in Fig. 3; or **Model II:** the **scaled length** of the leading geodesic depicted by ℓ_i in Fig. 3, i.e. the distance in the agents updated orientation direction to the boundary of its Voronoi cell. See Section 3.1.5 for a precise definitions. Intrinsic to both choices is a characteristic speed, here taken to be 1, fully accessible only when the personal space is sufficiently large (with respect to L).

2 Overview of Other Models

While, as we have just explained, the VTP model has a different motivation and flavour from the vast array of

models in active matter, we pause here to compare with a few important models. We first present three influential models achieving coherent behavior solely through symmetric alignment interactions. Vicsek et. al. introduced in [46] a simple kinematic model where, amid random noise, a transition to ordered behavior is obtained by averaging over the velocities of neighbors that fall within a metrically finite region, see [27] for analysis. Later Cucker and Smale introduced in [12] a flocking model (C-S) that, in contrast with Vicsek's, considers a global interaction where each agent is influenced by every other individual. Consequently, C-S presents conservation laws that, on one hand, fix the regimes through the initial conditions as for some physical system (e.g. thermodynamical) but, on the other, seem unreasonable for systems of cognitive, decision-making individuals. Another issue, pointed out by Motsch and Tadmor in [36], is that C-S invalidates the dynamics of small sub-flocks at long range; this problem is addressed in their model (M-T). Precisely, M-T introduces the notions of active sets to quantize neighbor's influence as well as the notion of relative distances. The latter being supported by the experiments on bird flocks due to Ballerini et. al. [4] demonstrating many flocking behaviors to be density invariant. As we will see, a (distinct) notion of relative distance is a direct consequence of our topological perception framework. Note these three approaches do not, in general, produce regimes other than velocity coherence. In this regard, much adapting has been done to produce aggregation and other biologically accurate behaviors by means of long range attraction, short range repulsion as well as hierarchy and leadership effects, see [20, 22, 13, 41, 9, 43, 1]. Other interesting variants include incorporating: (i) limited peripheral view [36], (ii) time delays accounting for limited processing aptitudes [17, 32], and (iii) active and passive distinction of agents [21, 8, 26, 28, 35]. Other important kinematic approaches which produce rolling and milling behaviors similar to ours are models of d'Orsogna et al. [14] and Bernoff-Topaz [45, 6] which consider attraction and repulsion through a potential as well as exogenous forces. The reader is also referred to seminal work done by Edelstein-Keshet et al. in the matter of modelling interactions through the potential formulation [33, 34, 16].

Particularly relevant to our approach is a family of models known as *zone-based* which generalize Vicsek's. Precisely, endogenous interactions act over non-overlapping concentric regions. Among this vast family one finds the popular boids model introduced by Reynolds in 1987 [42], a recent approach by Bernardi and Scianna (B-S) in [5] as well as the seminal Couzin model [11] with hierarchies between the different interactions; the Couzin model was later used in the context of effective leadership and propagation of directional awareness in [10]. Such zone based interactions are often realized as gradients of artificial potentials (although qualitative features often do not depend on the precise form of such potentials, e.g.

[30]) and this approach is seen in biological models as well as implemented in multi-agent control systems as in [29]. While our method can be perceived as zone-based under our Voronoi topology and recover similar coherent and cohesive regimes; there are fundamental differences. By design, in these other models, individuals steer toward the center of mass of other agents within interacting regions. However, we do not take the center of mass of spacial positions to be a natural object of consideration for agents. Despite this, we find similar behavior emerges for certain parameter regimes. Understanding the Voronoi cell as the agents' personal space within their local group, we argue that its geometry is in fact more natural than the center of mass of nearby agents. Another important distinction is our absence of long-range attraction between agents; ours is essentially a pedestrian (as opposed to swarming) model in the sense that we do not require nor encourage longevity of clusters of agents, rather we are interested in how agents navigate their environment and each other (with or without individual objectives).

Olfati-Saber and others have worked to present very broadly applicable theoretical frameworks for flocking in multi-agents systems in [40, 38, 39], especially for the case of linear dynamics (in both continuous and discrete time).

The "social force" pedestrian model (H-M) from Helbing and Molnár [25] (see also the seminal work [23]) strives for a realistic human pedestrian flow. Their cognitive assumptions align closely with ours, however, their formulation is rather different from ours and the models above in that it lacks the alignment feature. It too has no density-invariant communication notions. We believe that our model is conceptually much more natural and simpler, yet is capable of predicting similarly realistic behaviors (compare, e.g., Figure 8 with [25, Fig. 2] and with [47, Fig. 8]). Another problem with this and other microscopic models is the description in terms of *accelerations* of agents despite the fact that humans (unlike automobiles) can accelerate and brake almost instantaneously and that human agents do not think in terms of accelerations at the tactical level.

Finally, we emphasize that others have previously used Voronoi diagrams in multi-agent models and control systems and they feature prominently in the literature on epithelia and biological tissues [2, 7]. In [18], inspired by [4], Ginelli and Chaté show that adapting Vicsek's model to use a Voronoi communication graph produces qualitatively novel behaviors. In [20], Grégoire and Chaté describe a minimal extension of [18] which achieves selected coherent behaviors despite "unfavorable conditions". Where these use the Voronoi topology, the multi-vehicle control system developed by Lindhe et. al. in [31] considers a limited range neighbors, as Vicsek, but from these, constructs a Voronoi region whose geometry influences the control. Our model uses both the Voronoi topology and geometry to naturally synthesize many effects. We remark that in [44], Strandburg-Peshkin et. al. show that Voronoi based models empirically outperform

metrical and k -nearest-neighbor based models in the sense of information propagation through the network.

3 The Details of the VTP Models

We first recall the notions of the Voronoi diagram and Delaunay triangulation associated with a configuration of agents. Given a connected manifold Ω , an (extended) metric d on Ω , and set of distinct points $X = \{x_1, \dots, x_n\} \subset \Omega$, the d -Voronoi diagram in Ω generated by X is the almost disjoint collection $\text{VD}(X) = \{V_1, \dots, V_n\}$ where

$$V_i = \{x \in \Omega : d(x, x_i) < \infty \text{ and } d(x, x_i) \leq d(x, x_j) \text{ for all } 1 \leq j \leq n\}.$$

The regions V_i are called *Voronoi cells*. While in this paper d is always taken to be the Euclidean-measured geodesic distance on closed manifolds, see the last section for a discussion on using different metrics to incorporate more complex domain geometries.

The Voronoi diagram provides a natural dual structure to guide the inter-agent communication topology in our model. Given a set of generators $X = \{x_1, \dots, x_n\} \subset \Omega$ and the Voronoi diagram $\text{VD}(X)$ generated by X in Ω , its geometric dual graph² $\text{DT}(X)$ spans over the vertices X with nonempty edges e_{ij} if $\partial V_i \cap \partial V_j \neq \emptyset$. In the event that d is based on the Euclidian metric, $\text{DT}(X)$ is known as the Delaunay triangulation of X , see [37, 3]. We will often write $i \sim j$ to mean that x_i and x_j are adjacent in $\text{DT}(X)$, or equivalently, V_i and V_j share an edge.

3.1 Governing equations

While the model was designed with numerous generalizations in mind, we present it here in its simplest form. Our model includes (1) a connected domain Ω , (2) a finite index set Λ of agents, (3) positions $x_i = x_i(t) \in \Omega$ for each $i \in \Lambda$ such that $x_i(t) \neq x_j(t)$ for all t and for all $j \neq i$, and (4) closed (possibly empty) targets $T_i \subset \Omega$ for each $i \in \Lambda$. For each $i \in \Lambda$, we write $u_i(t) = x_i(t) - x_i(t-1)$.

Given initial conditions $x_i(0)$ and $u_i(0)$ (or equivalently $x_i(0)$ and $x_i(-1)$) for all $i \in \Lambda$ the system evolves according to an equation of the form³

$$x_i(t+1) = x_i(t) + f_i(X(t), U(t)) \quad \text{for all } i \in \Lambda \quad (1)$$

for functions $f_i : \Omega^n \times \mathbb{R}^{2n} \rightarrow \mathbb{R}^2$ where X and U are shorthand for $X(t) = (x_i(t) : i \in \Lambda)$ and $U(t) = (u_i(t) : i \in \Lambda)$ and $n = \#\Lambda$.

²Strictly speaking, $\text{DT}(X)$ is a *multigraph* with possibly multiple edges connecting the same pair of vertices. This occurs for certain topologies of Ω where a generator may “see” the same other generator on two or more sides of its own Voronoi cell.

³In full generality, this sum should be understood as a geodesic translation. I.e., $f_i : (T\Omega)^n \rightarrow T_{x_i(t)}\Omega$ considers n position-heading pairs in the tangent bundle $T\Omega$ and gives a tangent vector at x_i . Then, $x_i(t+1) = \Gamma_{i,t}(\lambda_i \|f_i(X(t), U(t))\|)$ where $\Gamma_{i,t} : \mathbb{R} \rightarrow \Omega$ is an isometric parametrization of the geodesic satisfying $\Gamma_{i,t}(0) = x_i(t)$ and $\Gamma'_{i,t}(0) = \alpha f_i(X(t), U(t))$ for some $\alpha > 0$.

So, the behavior of our model is then determined by the precise nature of f_i . Because we assume each agent has only local information, f_i will only depend on a narrow subset of agents (those adjacent in $\text{DT}(X)$) at each instant but their identities will change over time in general. The functions $f_i : \Omega^n \times \mathbb{R}^{2n} \rightarrow \mathbb{R}^2$ are given by

$$f_i(X, U) = \rho_i d_i, \quad d_i = \frac{\sigma_i r_i + \nu a_i + \bar{\sigma}_i h_i}{\sigma_i + \nu + b_i \bar{\sigma}_i}. \quad (2)$$

Here, d_i is a weighted combination of three components r_i , a_i , h_i , *repulsion*, *alignment*, and *homing*, respectively, with nonnegative coefficients σ_i , ν , and $\bar{\sigma}_i$. (The factor $b_i \in \{0, 1\}$ is 1 unless the target T_i is empty or contains i ’s current position.) Definitions of r_i , a_i , and h_i are given in Equations (3,5,6) and the weights σ_i , $\bar{\sigma}_i$ in (7). We then scale by ρ_i which depends on i ’s personal space and is defined later in (8). Repulsion, alignment, and homing are shown schematically in Figure 2. We remark that (2) does not present a magnitude/direction decomposition as d_i is not in general a unit vector. In a sense, d_i encapsulates the external influences on i while ρ_i gives the speed scale i would like to achieve if allowed by d_i . Because of this, f_i can be small for two very different reasons: ρ_i will be small when i has very little room to move and d_i will be small if repulsion, alignment, and homing nearly cancel each other. However, $\|d_i\|$ is on average bounded above by $1 + 1/\nu$ (c.f. Appendix), thus making d_i a physically sensible direction of motion.

3.1.1 Repulsion vector r_i

The repulsion term r_i , illustrated in Figure 2b, is a collision-avoidance mechanism motivated by the *move-away-from-closest-neighbor* dynamics (MACN) used in the context of Voronoi energy minimization in [19]. Specifically, given positions $X = (x_1, \dots, x_n) \in \Omega^n$, the repulsion vectors r_i are given by the average of unit vectors

$$r_i(X) = \frac{1}{\#K_i} \sum_{y \in K_i} \frac{x_i - y}{\|x_i - y\|} \quad (3)$$

where K_i is the set of distance minimizers among all “obstacles”. Here the word obstacles refers to the other agents and the domain boundary, if it exists. Precisely, $K_i = K_i(X) = \{y \in \Omega : \|x_i - y\| = \inf_w \|x_i - w\|\}$ where the infimum is taken over $w \in \{x_j : j \neq i\} \cup \partial\Omega$, the other points in the tuple X and boundary points of Ω . In the typical case, K_i contains exactly one element, namely, the nearest obstacle to x_i , in which case r_i is simply the unit vector at x_i pointing away from the obstacle, but we define r_i to account in the obvious way for edge cases when x_i is equidistant from two or more obstacles.

We also define $\delta_i := \text{dist}(x_i, K_i) = \|x_i - y\|$ for all $y \in K_i$ to be the unique distance from x_i to its nearest obstacle(s), as indicated in Figure 2b.

For many parameter ranges there is a short time oscillatory structure to r_i resulting from nearest-neighbor connectivity changes in $\text{DT}(X)$ (see [19] for more details). In

these cases, the late-time animations show a “jittering” in the individual agents direction. We do not see this as a weakness in our model as agents on a small timescale may very well have a frenetic nature which averages out over large temporal and spatial scales.

3.1.2 Alignment vector a_i

Alignment is illustrated schematically in Figure 2c. Given $X = (x_1, \dots, x_n) \in \Omega^n$, we write $j \sim i$ to mean that x_j and x_i are adjacent in $\text{DT}(X)$, or equivalently, that their Voronoi cells V_j and V_i share an edge. Then, for positions $X = (x_1, \dots, x_n) \in \Omega^n$ and headings $U = (u_1, \dots, u_n) \in \mathbb{R}^{2n}$, we define the *alignment vector* \tilde{a}_i by the weighted average

$$\tilde{a}_i = \tilde{a}_i(X, U) = \frac{1}{\deg_{\text{DT}(X)}(x_i)} \sum_{j \sim i} g(\theta_{ij}) \hat{u}_j \quad (4)$$

where $\deg_G(v)$ denotes the degree of vertex v in a graph G ; $\hat{u}_j = u_j / \|u_j\|$; and $\theta_{ij} = \arccos(\hat{u}_i \cdot \hat{u}_j)$ is the angle between u_i and u_j . Here $g : [0, \pi] \rightarrow [0, 1]$ is a continuous non-increasing function with $g(0) = 1$ and $g(\pi) = 0$. Thus, agent i considers the *orientation* of each of its neighbors and averages these, favoring those whose direction is consistent with its own (θ_{ij} near 0) and virtually ignoring those whose direction is opposed (θ_{ij} close to π). The role of the weighting g (more specifically its behavior near 0 and 1) is crucial because it allows the model to tolerate very high sheer in the flow despite the averaging of orientations. Put another way, the fact that agents can move in opposition to one another without much affecting this term manifests in interesting ways dynamically. E.g., two opposing streams, if sufficiently sparse that repulsion is small, can pass through each other relatively easily with agents in each stream ignoring those in the other stream while reinforcing others in their own stream. However, an agent approaching a transversely moving group of others will be significantly deflected by it. We will see later what we call *anti-cog* collective behavior which exhibits very high sheer in the flow and does not occur without the falloff of g at π . We will also see two-way flow wherein non-jamming behaviors are much more accessible due to the weighting g .

We define the *alignment coefficient* φ_i by $\varphi_i(X) = \frac{1}{6} \deg_{\text{DT}(X)}(x_i)$. To motivate this definition, we note that in any Voronoi diagram (in the torus, sphere, plane, or planar region), a typical cell has at most six neighboring cells (c.f. Appendix). So φ_i captures how “surrounded” x_i is in the $\text{DT}(X)$ topology. We then write

$$a_i = \varphi_i \tilde{a}_i = \frac{1}{6} \sum_{j \sim i} g(\theta_{ij}) \hat{u}_j. \quad (5)$$

The effect of scaling by φ_i is that agents with relatively few neighbors will be less strongly affected by this alignment interaction. Conversely, without φ_i , the alignment component of i would be crippled whenever i has many

neighbors moving in the opposite direction. Overall, introducing φ_i mimics in outcome the improvement of *relative distance* brought by [36] over [12].

Noticing that alignment at time t depends on $\text{DT}(X(t))$, one may point out that since the previous time step $t - 1$, the communication topology $j \sim i$ may have changed. In particular, the $\text{DT}(X(t))$ -neighborhood of $x_i(t)$ may include an agent who did not neighbor agent i at $t - 1$ (and was therefore invisible to them at the time); yet, according to (5), agent i is expected to have orientation information about that agent. We argue however that this seemingly cognitively expensive assumption on our population does not in fact require agents to have any memory at all; the only assumption made is that every agent is able to infer the orientation of their neighbors from their current body geometry in a trivial amount of time, e.g. by looking at their noses, tails, etc. Concretely, at time t , agent $x_i(t)$ looks at all $j \sim i$ in $\text{DT}(X(t))$ and gauges their orientation $\{\hat{u}_j\}_{j \sim i}$ based on body geometry alone but does not need to infer any speed information $\{\|u_j\|\}_{j \sim i}$. Should the latter be the case, then agents would indeed need memory of their neighbors’ positions $\{x_j(t - 1)\}$ at earlier time. Thus, under our simple assumption on body geometry assessment, using unit length orientations as opposed to velocity vectors in (5) indeed makes our model cognitively cheap and memoryless.

At last, we refer the reader to the Appendix where a simple linearisation of (4) shows that our alignment component incorporates three main terms: an inertial term aiming to preserve the heading of each agent i , a “traditional” unweighted average of the neighbors’ orientation and a third “curling” term containing the nonlinear influence of the neighbors $j \sim i$ onto i .

3.1.3 Homing vector h_i

The homing term is shown for a simple point-target in Figure 2a. This term simply points from $x_i \in \Omega$ toward the target point T_i . We define the target point $x_i^* \in T_i$ by $\|x_i^* - x_i\| = \text{dist}(x_i, T_i)$. There is in general an issue of uniqueness here but in practice, this ambiguity is inconsequential because the set on which this definition is ambiguous has measure zero in Ω . The *unit homing vector* \hat{h}_i is given by

$$\hat{h}_i(X) = \frac{x_i^* - x_i}{\|x_i^* - x_i\|} \quad \text{for } x_i \notin T_i \quad (6)$$

To account for the possibilities that $x_i \in T_i$ or $T_i = \emptyset$, we define the factor b_i to be 0 if $x_i \in T_i$ or $T_i = \emptyset$ and 1 otherwise and write $h_i = b_i \hat{h}_i$ so that $h_i = 0$ when \hat{h}_i is ill-defined.

3.1.4 Weighting coefficients σ, ν and b_i

The weighting coefficients in (2) are defined as follows. The repulsion r_i and homing h_i appear with weights σ_i

and $\bar{\sigma}_i$ and these are defined by introducing the length scale L and a *repulsion cut off function* $\sigma(\cdot)$. We refer to L as the *repulsive falloff distance* which can also be used to capture the size of the agents. Precisely, we define the convexly related terms

$$\sigma_i = \sigma(\delta_i/L) \quad \text{and} \quad \bar{\sigma}_i = 1 - \sigma_i = 1 - \sigma(\delta_i/L) \quad (7)$$

where $\sigma : [0, \infty) \rightarrow [0, 1]$ is⁴ continuous at 0, non-increasing, and satisfies $\sigma(0) = 1$ and $\sigma(1) = 0$. Here $L > 0$ is a parameter of our model we refer to as the *repulsive falloff distance*. Thus, recalling that δ_i is the distance from x_i to its nearest agent (or boundary), we see that the convex combination $\sigma_i r_i + \bar{\sigma}_i h_i$ facilitates the following behavior. If x_i is at least a distance L from all obstacles, then full priority is given to target-seeking via h_i . On the other hand, as obstacles encroach on x_i at distances less than L , collision avoidance via r_i takes priority over target seeking.

The remaining coefficient $\nu \geq 0$ in (2) determines the overall strength of the alignment effect compared to the combined homing-repulsion effect.

3.1.5 Personal-space speed

The scalar ρ_i in (2) refines the step size based upon agent i 's personal space, and essentially sets the agents speed. Model I is based on the area of the visible personal-space. Precisely, let for $x_i, u_i \in \mathbb{R}^2$, define $H(x_i, u_i) = \{x_i + w \in \mathbb{R}^2 : u_i \cdot w \geq 0\}$ to be the half plane with normal parallel to u_i whose boundary contains x_i . Then for $X = (x_1, \dots, x_n) \in \Omega^n$ and $U = (u_1, \dots, u_n) \in \mathbb{R}^{2n}$ and Voronoi diagram $\{V_1, \dots, V_n\}$, define⁵

$$F_i = F_i(X, U) = \begin{cases} \text{area}(V_i \cap H(x_i, u_i)) & \text{if } u_i \neq 0, \\ \frac{1}{2} \text{area}(V_i) & \text{if } u_i = 0. \end{cases}$$

To nondimensionalize F_i , we use the length scale L we have already introduced, the repulsive falloff distance, and consider the quantity $\frac{F_i}{\pi L^2/2}$, rescaling F_i by the area of the semicircle of radius L .⁶ Finally, to obtain a step size from this quantity which is physically reasonable, we must enclose it in an increasing function that behaves like the identity near zero and goes to unity asymptotically so that agents attain maximum speed of 1 when there is nothing in their way. For this we take the hyperbolic tangent. Thus for Model I, the coefficient ρ_i is given by

$$\rho_i = \rho_i(X, U) = \tanh\left(\frac{F_i}{\pi L^2/2}\right). \quad (8)$$

⁴We take $\sigma(s) = \frac{z(1-s)}{z(s)+z(1-s)}$ where $z(s) = \exp(-1/s)\chi_{(0,\infty)}(s)$ and $g(s) = \sigma(s/\pi)$.

⁵To motivate the $u_i = 0$ case, we employ a probabilistic argument. The expected value of $V \cap H(x_i, u_i)$ for arbitrary x_i and measurable set V over u_i from a radially symmetric distribution is half the measure of V . The proof is given in the appendix.

⁶On the sphere $\Omega = R\mathbb{S}^2$, we define F_i in the analogous way. For $(x_i, u_i) \in T\Omega$ in the tangent bundle, taking $H(x_i, u_i)$ to be the *hemisphere* whose bounding great circle γ includes x_i and whose tangent at x_i is orthogonal to u_i . We then rescale F_i by half the area of a spherical cap of geodesic radius $L \in [0, \pi R]$.

rescales the step size. Model II follows the same reasonings but is based upon, ℓ_i , the length of the segment starting at the position x_i in the direction u_i to the boundary of the Voronoi cell of x_i . For Model II the coefficient ρ_i is given by

$$\rho_i = \rho_i(X, U) = \tanh\left(\frac{\ell_i}{L}\right). \quad (9)$$

3.1.6 Summary of the parameters

To summarize, our model involves two fundamental **control parameters**: the alignment coefficient ν and the repulsive falloff distance L . There will be two other parameters; another length scale L_s for the bidirectional corridor wherein agents enter according to a prescribed process, and μ , a dimensionless version of L for compact domains without boundary. The number of agents n is also a parameter but we confine our study to n between 500 and 1000. All the other “weights” are directly determined by the local Voronoi geometry, modulo transitions functions σ (for the weighting of repulsion with homing), g (for weighting neighbouring agent alignment), and \tanh (for speed adjustment in ρ_i); for the former two we made canonical choices. We note that there are two additional *parameters* which have been set to unity: the time step and a *characteristic speed* intrinsic in our definitions of σ and ρ_i .

4 Single-point Target in the Plane

4.1 Observables

To quantify our simulations in the various regimes, we consider comparable observables in addition to the angular momentum. Namely, the mean-median (relative) radius given by

$$r_{\text{mm}} = \frac{1}{L} \text{mean median}_{1 \leq i \leq N} |x_i(t) - \bar{x}(t)|$$

where $\bar{x}(t)$ is the center of mass at time t . This gives a measure of the average size of the swarm which is insensitive to outliers.

We introduce a global *pressure* defined in terms of the Voronoi diagram. Namely,

$$P(X) = \frac{1}{n} \sum_i \frac{1}{|V_i|},$$

where $n = |X|$ and $|V_i|$ is the area of the Voronoi cell containing $x_i \in X$ in the diagram generated by X . In the case that $|V_i| = \infty$, it is understood that $1/|V_i| = 0$. This mean reciprocal area is analogous to pressure in the following way. A back-of-the-envelope calculation (see below) suggests that, under certain regularity assumptions, if the bounded parts of two Voronoi diagrams fill the same volume, then the denser configuration, i.e., the

one with more generators, has the larger mean reciprocal area and this relationship is sublinear, being closest to linear when there are many more bounded than unbounded cells. Moreover, we have the following scaling relationship $P(rX) = \frac{1}{|r|^d} P(X)$ in \mathbb{R}^d . So we have an analogue of the familiar proportionality $P \propto n/V$ between pressure, number, and total volume (even though we are in an unbounded domain).

The “back-of-the-envelope” calculation suggested above is as follows. Let $\{V_i\}_{1 \leq i \leq n}$ be a Voronoi diagram in \mathbb{R}^d whose bounded part has total volume V . Without loss of generality, say $\{V_i\}_{i \leq n_0}$ are all and only the bounded cells for some $n_0 < n$. Suppose that the bounded cells are equi-distributed in the sense that $|V_i| = V/n_0$ for each $1 \leq i \leq n_0$. Of course, this assumption is almost impossibly restrictive but one can argue the the pressure is stable under small perturbations. **This argument is included in the appendix.**⁷ The pressure is given by

$$P = \frac{1}{n} \sum_i \frac{1}{|V_i|} = \frac{1}{n} \sum_{i \leq n_0} \frac{1}{|V_i|} = \frac{1}{n} \sum_{i \leq n_0} \frac{n_0}{V} = \frac{n_0}{n} \frac{n_0}{V}.$$

If $n_0 \sim n - Cn^{1/d}$, as is typical. Then fixing V , we have

$$PV \sim \frac{(n - Cn^{1/d})^2}{n} = n - O(n^{1/d})$$

where the error term $O(n^{1/d})$ is positive.

4.2 Results

Since the domain \mathbb{R}^2 with a single point-target is invariant under scaling, one might be tempted to conclude our choice of the repulsive falloff distance L is inconsequential⁸. While this is not exactly the case, we set $L = 1$ for our analysis of the single point target and refer to the appendix for further explanation/justification. With $L = 1$ fixed, we study empirically the long-term evolution of the system for different numbers of agents n and values of the alignment strength ν . We take as the initial state uniformly random positions within a square of area $n/2$ centered about the target point and unit velocities with uniformly random directions (the initial speed has no effect on the model since the previous speed is forgotten at each step). The long term dynamics are robust to the initial conditions; we chose a square simply because (pseudo)random points in a square are easily generated. The area of $n/2$ is comparable to the eventual size of the swarm (for a wide range of values of ν) and so this choice shortens the transient. The choice here which most significantly affects the dynamics is having the initial configuration centered on the target. Even if this is not so,

⁷Specifically, by first restricting to a sufficiently large closed ball including the bounded part of the voronoi diagram and change, one can argue that for any ε small enough, there exists $\delta > 0$ such that if $\|x_i - \tilde{x}_i\| < \delta$ for each i and \tilde{x}_i is in the convex hull of the perturbed points if and only if x_i belongs to the convex hull of the original points, then $(1 + \varepsilon)^{-1} P \leq \tilde{P} \leq (1 - \varepsilon)^{-1} P$.

⁸Simulations on the VTP site for point targets on compact manifolds without boundary do vary L .

we have found the long term behaviour to be robust but having the target point outside the initial swarm often results in transient regimes lasting hundreds or thousands of iterations. For both Models I and II, for small ν , the homing effect drives the swarm into a disc centered on the target and the velocities are uncorrelated. The equilibrium density of this disc is about where homing and repulsion are balanced and this depends on the shape of the falloff function for repulsion. For very large ν , the swarm forms a rolling cluster which itself orbits the target point while individuals make periodic near passes to the target point. Due the the strong alignment, agents are very nearly aligned at each fixed time.

The intermediate values of ν observe more interesting dynamics. First let us address Model II in which speed updates depend on the length of the leading straight geodesic. Increasing ν from the lower extreme, one sees an increase in the angular momentum (with respect to the center of mass and to the target) achieved by the the swarm (after an initial transient) as the velocities become more correlated. Enter the *pinwheel* regime. The agents occupy a disc whose center averages near the target with roughly uniform density and rotate in the same direction about the target. Agents on the outer edge of the swam tend to move faster than others, having relatively long leading geodesics. Further increasing ν , the center of the pinwheel becomes unstable and a cavity opens up, entering the *ring* regime. The rings form robustly in after a typical transient of a few hundred iterations for sufficiently small ν , with the ring diameter increasing with ν for each fixed n . However, one can coax the swarm into still larger rings at greater values of ν by first lowering and then gradually increasing ν during the simulation. The stability of these large coerced rings in unclear.

Model I, in which speed depends on the area of the leading straight cone, exhibits qualitatively different dynamics in the intermediate ν regime which we refer as a *breathing regime*. Here, like model II, the swarm forms a vortex about the target (after a short transient) and this vortex is filled for small ν and cavitated for larger ν . Unlike model I, the size of the vortex is not constant in time. Rather, the cavity slowly grows over time between intermittent “inspiral collapses”. The slow growth of the ring seems in part due to the fact that agents on the outer edge tend to have extremely large (or infinitely large) leading straight cones, and so move at nearly top speed, much faster than their inner neighbors. This speed difference causes the outermost agents to spiral further outward which in turn enlarges the Voronoi cells and leading cones of their inner neighbors, propagating the speed increase inward. But as the central cavity grows, so do the Voronoi cells of the innermost agents. The collapses occur when an agent on the inner edge of the ring deviates toward the center (e.g., due to repulsion from an outer neighbor) and, having large straight cone, deviates significantly. This effect propagates backward through alignment and the resulting enlargement in the Voronoi

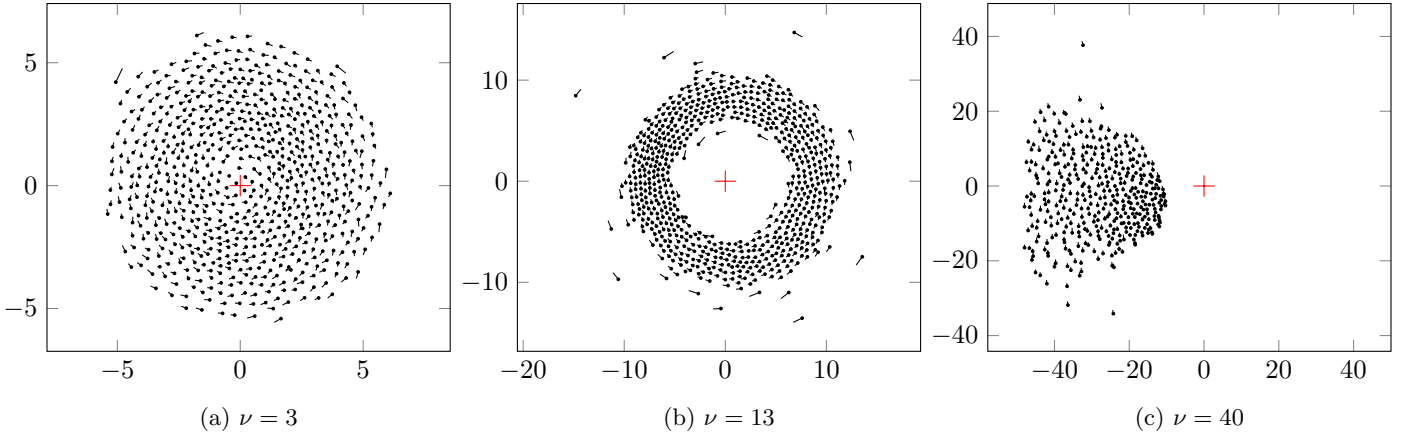


Figure 4: Pinwheel (a), ring (b), and aligned orbiting cluster (c) for $N = 700$ agents under Model II. The red crosshairs indicates the target point.

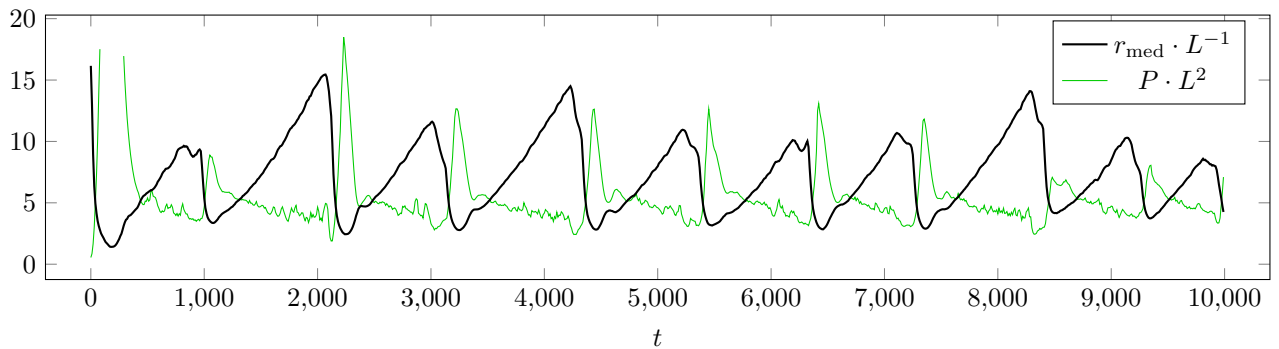


Figure 5: Example of the *breathing regime* observed under Model I. Here there are $N = 700$ agents and the alignment strength is $\nu = 8$. The curve (black) is the median radius of all agents (against time), i.e., the median distance to the center of mass of the swarm. The secondary curve (green) is the Voronoi pressure. Each is nondimensionalized with a suitable power of L (although here $L = 1$). The initial spike in pressure is clipped for space but the maximum is approximately 60.

cells of trailing neighbors.

(stochastic) process governing the sources is discussed in the Appendix.

5 The Bidirectional Hallway

To showcase how our VTP framework naturally adapts to sources and sinks, we address its predictions (for Model I) in a narrow corridor Ω with two subpopulations looking to enter by each end and exit through the opposite one while interfering with each other throughout their crossing. Specifically; Ω is represented by a rectangle of width 1 and large enough length, the number of agents $n = n(t) = \#\Lambda(t)$ varies since the index set $\Lambda(t) := \Lambda_r(t) \cup \Lambda_l(t)$ of all agents inside the hallway is no longer constant in time and consists of agents $X_r := \{x_i(t)\}_{i \in \Lambda_r(t)}$ entering by its left edge and targeting its right edge –i.e. the entire right side represents T_i for $i \in \Lambda_r$. The subgroup $X_l := \{x_i(t)\}_{i \in \Lambda_l(t)}$ moving from right to left is defined analogously. Note that once an agent enters it can only exit through its corresponding target as all three other walls repel. Details of the

5.1 Observables

To quantify the distinct behaviors exhibited by this bidirectional flow, we employ the following observables:

First the *polarization* proper to each subgroup

$$S_{r,l}(U) := \frac{1}{\#\Lambda_{r,l}} \left\| \sum_{i \in \Lambda_{r,l}} \hat{u}_i \right\|$$

This is a simple yet efficient order parameter widely used in the literature to measure heading consensus. Note that $0 \leq S_{r,l} \leq 1$ and that we measure it for each subgroup individually since the global polarization taken over $i \in \Lambda$ is expected to be systematically small due to the symmetry of the scenario. We then measure overall polarization with $S := \frac{1}{2}(S_r + S_l)$.

Better suited to a bounded domain than the pressure

P , we use the *clustering energy*

$$E(X) := \frac{n \cdot 18\sqrt{3}}{5|\Omega|^2} \sum_{i \in \Lambda} \int_{V_i} ||x - x_i||^2 dx$$

to infer on the overall spatial distribution of agents. As opposed to the Voronoi pressure from §4.1 this function measures the variances of $\{V_i\}_{i \in \Lambda}$ with respect to $\{x_i\}_{i \in \Lambda}$ and thus, as agents are “better centered” within their own Voronoi regions, the value of E decreases. Although this quantity arises frequently apropos of centroidal Voronoi tessellations (see [15]); to our knowledge, it has so far been absent in the vast literature of collective behavior. While E has several remarkable properties and the reader is referred to [19] for more detail, we limit ourselves to point out that the factor $\frac{n \cdot 18\sqrt{3}}{5|\Omega|^2}$ is a scaling allowing to compare values of E as $n(t)$ changes and that $E(X) \geq 1$ for any spatial configuration X .

To quantify *percolation*, i.e. the extent to which agents of a subgroup entwine and venture into the other subgroup, we define the *Voronoi interface length*

$$I(X) := \sum_{i \in \Lambda_r; j \in \Lambda_l} |\partial V_i \cap \partial V_j|$$

which is simply the total Euclidian length of the boundary having Voronoi cells generated by Λ_r on one side and by Λ_l on the other.

Finally, a key structural behavior that we wish to shed light on is *queuing*. Namely, we wish to quantify a very specific type of ordered behavior among agents of the **same group** who not only exhibit orientation consensus and certain spatial cohesion but also “align behind each other” to form *lanes* oriented along the path towards their common target. To this end, we define *queuing structures* \mathcal{Q}_r and \mathcal{Q}_l that inherit part of the topology from $\text{DT}(X)$ and also incorporate geometrical features about the current state $(X_i; U_i)_{i \in \Lambda_r, l}$; subsequently, an observable $Q(\mathcal{Q}_{r, l})$ that measures their “queuing quality” is defined.

Although, any definition making up a reasonable queuing structure is highly subjective and open to debate; we postulate that the graph \mathcal{Q}_r (and its analogous \mathcal{Q}_l) need to verify at least these four properties to intuitively showcase lane formations:

- i) \mathcal{Q}_r is a subgraph of \mathcal{D}_r , the restriction of $\text{DT}(X)$ to the vertices X_r . Note that, in general, $\mathcal{D}_r \neq \text{DT}(X_r)$.
- ii) \mathcal{Q}_r has $\deg_{\mathcal{Q}_r}(x_i) = 1, 2$ for all $x_i \in \text{vert}(\mathcal{Q}_r)$.
- iii) \mathcal{Q}_r is a forest, i.e. a (disconnected) acyclic graph.
- iv) the edges $\{e_k\}$ of \mathcal{Q}_r are endowed with nonnegative weights $\{w_k\}$ where w_k is smallest whenever $e_k = (x_{i_k}, x_{j_k})$ and the endpoint velocities u_{i_k}, u_{j_k} are all collinear to the common homing direction \hat{h} .

The intuition behind these requirements is that, after identifying each connected component of $\mathcal{Q}_{r, l}$ with a **distinct lane**:

- i) two agents are contiguous in a lane only if they are from the same subpopulation and are connected in $\text{DT}(X)$ (and thus may interact via repulsion and alignment).
- ii) a lane has no singleton vertices and is not ramified.
- iii) a lane does not close on itself.
- iv) we can locally quantify lane edges based on three simple geometrical elements; the moving direction of the endpoint agents, their relative position and their homing. The smaller the weight, the more in sync the pair of agents is towards their target.

We refer to the appendix for details on the ad hoc construction of $\mathcal{Q}_{r, l}$ we used in our work below and stress that there are, in general, many different graphs satisfying these postulates at any given time t . Results can thus fluctuate as variations in the construction are explored. At last, let $\{\mathcal{L}_m(\mathcal{Q}_r)\}_{m=1}^M$ represent the collection of M lanes composing \mathcal{Q}_r (i.e. its connected components), then we define the *queuing observable* $Q_r = Q(\mathcal{Q}_r)$ by

$$Q_r := \frac{n}{\#\text{vert}(\mathcal{Q}_r)} \frac{1}{M} \sum_{m=1}^M \frac{1}{[\#\text{edge}(\mathcal{L}_m(\mathcal{Q}_r))]^2} \sum_{e_k \in \mathcal{L}_m(\mathcal{Q}_r)} w_k$$

Indeed, this quantifies queuing according to four criteria: number of lanes M , overall number of edges of each lane (i.e. topological length of lanes), overall weight of each lane and number of agents belonging to \mathcal{Q}_r . As each one of these individual criteria improves while keeping the other three fixed, the value of Q_r decreases. Thus it is sensible to associate “good” queuing with **ever lower values of Q_r** .

We define \mathcal{Q}_l and $Q_l = Q(\mathcal{Q}_l)$ analogously; the overall amount of queuing in the hallway at any given time is then captured using $Q := \frac{1}{2}(Q_r + Q_l)$.

In conclusion, besides the classical *polarization*, we have introduced observables to measure *clustering*, *percolation* and *queuing* that take advantage and very naturally combine the Voronoi/Delaunay topology intrinsic to our model with elementary geometric features (position, angles and distances).

5.2 Results

To model the sources, we capture the degree of freedom underlying the inflow by a parameter L_s called the *source length scale* that accounts for the agents’ preferred interpersonal distance near the entrances. Specifically, if there is a half disk of radius L_s centered somewhere on the entrance that is devoided of any agents, there is a large

probability that a new agent will enter through that gap. Thus, the **smaller** L_s is, the **larger** the influx.

Full detail on this stochastic entry process is presented in the Appendix but we remark that: i) the inflow rate is not constant and will diminish as the hallway is obstructed near the sources, ii) using L_s to quantify inflow allows for a convenient comparison with the intrinsic length scale L .

Consequently, on top of our model's parameters ν and L , the exogenous quantity L_s also plays a crucial role in the dynamics. However, we claim that to qualitatively survey the emergent behaviors, one can categorize ν as either “weak” or “strong” and focus on (L, L_s) , where:

- weak alignment dynamics ($0 < \nu \leq 1$) are dominated by repulsion and homing, thus L and L_s take precedence over ν .
- strong alignment ($\nu \geq 2$) renders the influences of L and L_s harder to predict. As will be presented below; larger ν values are characterised by the presence of vorticity due to nonnegligible counterflow sheer.

We emphasize that, as opposed to the case $\Omega = \mathbb{R}^2$ from §4, the now present size effects make little to no qualitative difference between using Model I and Model II. In other words, as part of our observations, we encountered that having a non-negligible agent density on a restricted space produces very similar outcomes when agents base their speed upon personal forward area F_i or on personal distance ahead ℓ_i .

For thoroughness we included the results obtained with Model II in the Appendix but the remainder of §5 will focus on Model I.

5.2.1 Weak alignment

Figure 6 presents the phase diagram (L, L_s) for $\nu = 1$ under several quantities. The maximal number of agents allowed to enter Ω was set to 1000 at each source and the dynamics evolved over $t = 1, \dots, 1500$ iterations.

The four observables shown are averaged over the tail $t \in [500; 1500]$ to avoid any transient.

When looking at the number of agents that entered and exited by the time $t_{max} = 1500$, a clear bifurcation line γ_{1500} emerges where, on one side the inflow is large enough (L_s small enough) to produce a complete occlusion of the hallway and, on the other side we see a full crossing of Ω since (almost) all agents having entered manage to exit through their respective target. The bifurcation line was numerically found to be

$$\gamma_{1500} : L_s = 1.93 L + 1.7 \cdot 10^{-3}$$

Remarkably, γ_{1500} also signals a sharp transition under each of the four observables we defined in §5.1; clearly the nontrivial dynamics are found over $L_s \geq \gamma_{1500}$ where large polarization S and low clustering E indicate long lasting and orderly migration uniformly distributed in

space.

Furthermore, over the same region, percolation I decreases with L_s while the overall queuing Q is optimal when closest to γ_{1500} and increases again as we stray away from the bifurcation. The latter increase in Q is to be expected since our alignment components $\{a_i\}$ (eq. 5) only consider orientation and not position; thus according to this modelling choice, as the density in the hallway decreases (increase in L_s), agents are no longer prompt to press together and organise in lanes. Conversely, the smooth gradient of Q we observe above γ_{1500} in Figure 6 comes to validate our definitions for \mathcal{Q} and Q as being sensible constructions of what can intuitively be considered queuing.

Note that the measurements made for weak alignment are robust under change of the random generator of the entry process.

At last, since our simulations are carried out in finite time and with finite maximal number of agents entering Ω , the bifurcation we measured may very well change with either quantity. Specifically, while the transition curve from complete occlusion to full migration can only move upwards in the phase diagram as we increase the time evolution of the dynamics; we conjecture that, as $t_{max} \rightarrow \infty$ and with an infinite number agents at disposal, there exists a limiting curve γ_∞ representing the “true” critical bifurcation between eventual occlusion and sustained migration.

We conclude on weak alignment with four specific regimes (I)-(IV) produced with $L = \frac{1}{12}$; their main characteristics are listed below and the animations of their time evolution are found in the Github site:

- (I) here $L_s = 0.1875$ is above the theoretical γ_∞ and shows a large sustained percolation from the beginning, we're in the optimal queuing region (lowest Q values).
- (II) is very similar to (I) in the long term with the difference that $L_s = 0.175$ being slightly smaller (larger influx) forces a turbulent transient before a long lasting equilibrium with great queuing is established.
- (III) here $L_s = 0.1687$ is found between γ_{1500} and γ_∞ , meaning that a full occlusion eventually settles sometime after $t_{max} = 1500$. Nonetheless, for $t \leq t_{max}$ we see an interesting mixture of percolation, queuing and turbulence.
- (IV) $L_s \ll \gamma_{1500}$ produces a trivial regime where full occlusion settles in very fast and no interesting formations emerge.

Note that, by changing L we obtain similar qualitative behaviors as above provided L_s is found in the corresponding regions, i.e. the behaviors remain comparable but with a more or less densely populated corridor.

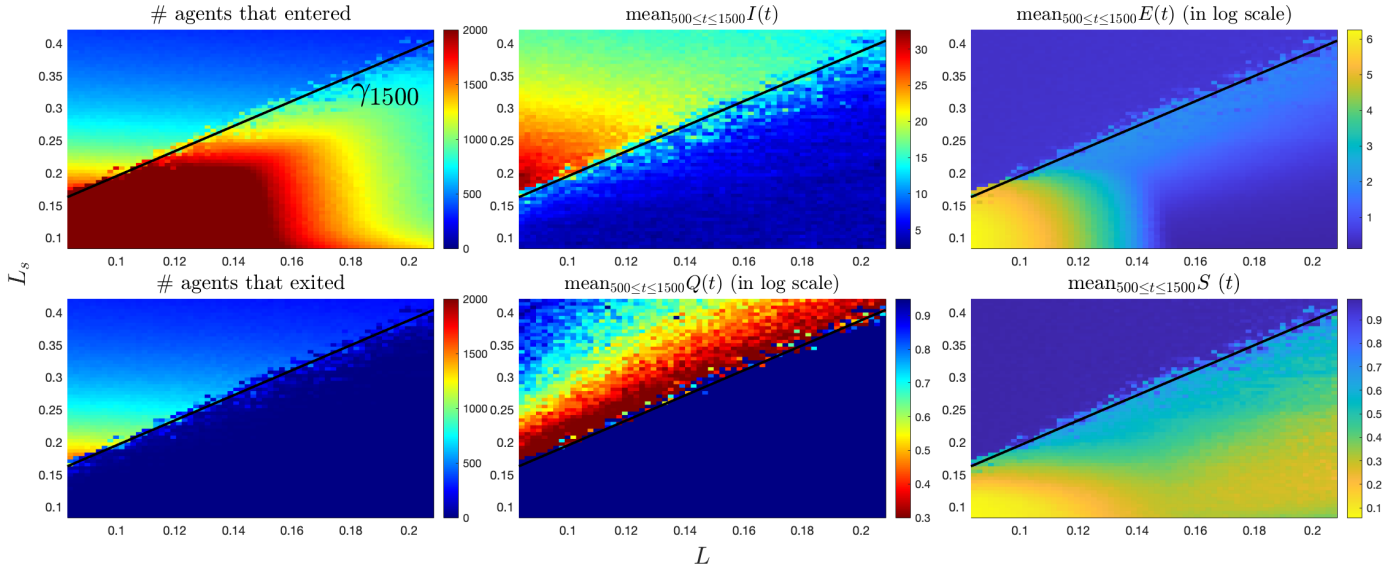


Figure 6: Phase diagram (L, L_s) for **Model I** on the bidirectional hallway under weak alignment $\nu = 1$ (with resolution of 65×65 points). The four observables I, Q, E and S from §5.1 are averaged over the time tail $t \in [500; 1500]$.

When looking at the number of agents that entered and exited by the time $t_{max} = 1500$, a sharp bifurcation $\gamma_{1500} : L_s = 1.93 L + 1.7 \cdot 10^{-3}$ emerges (*left column*). Remarkably, the same line shows a clear phase transition under each of our four observables. The region $L_s \geq \gamma_{1500}$ is characterized by the same number of entering and exiting agents as well as small E and large I ; this translates to long-lasting sustained migrations with agents uniformly distributed. Moreover, the smooth increase of Q away from γ_{1500} comes to further validate our postulates for $Q_{r,l}$ as producing a sensible notion for queuing.

5.2.2 Strong alignment

Compared to week alignment, the case $\nu \geq 2$ exhibits dynamics that are not as predictable. While the two extreme cases, i.e. L_s sufficiently large and sufficiently small, still produce steady unobstructed migrations and full obstructions respectively; the transition from one to the other is quite blurry and significantly richer in dynamics thanks to the sheering effects capable of producing a large amounts of vorticity.

Figure 7 shows the (L, L_s) phase diagram for $\nu = 2$ where the maximal number of agents allowed to enter Ω was set to 1500 at each source and the dynamics evolved again over $t = 1, \dots, 1500$. There a dashed gray line indicates where the blurry transition away from the steady migration region begins. We remark for the sake of thoroughness that the data was found to be robust under the random entry generator of agents for the region above the gray line but not below it.

Although lacking a well established and robust region in the phase diagram, we have identified one persistent emergent behavior famously known in the literature (see, for example, [48]) where

- (V) each subgroup flows on respective sides of the corridor creating almost no percolation and an interface between them along the length of the hallway.

This regime is shown in Figure 8 (*bottom*), it reminds of

a separated two-phase fluid flow along a pipe.

To show the reader other observed behaviors, the Github site also contains these regimes:

- (VI) with $\nu = 2$ where one subgroup overcomes and manages to split the flow of the other in two; thus creating two interfaces along the length of the corridor. Here the (L, L_s) values are in the blurry transition region showcased in Figure 8.
- (VII) with $\nu = 5$ where vorticity completely dominates. This is visually more resemblant to the growing and collapsing of mills in §4 than to an ordered flow.

To conclude with the bidirectional corridor we remark that, although the orientation of agents can be rather noisy when clustered together due to the nature of the repulsion components $\{r_i\}$, the dynamics do average out over medium time scales and avoid the "freezing by heating" effect known to disrupt all lane formation when noise is too great, see [24].

6 Compact Domains without Boundary

We have adapted VTP (Model I) to two compact domains Ω without boundary, the square torus $\mathbb{R}^2/l\mathbb{Z}^2$ of primary

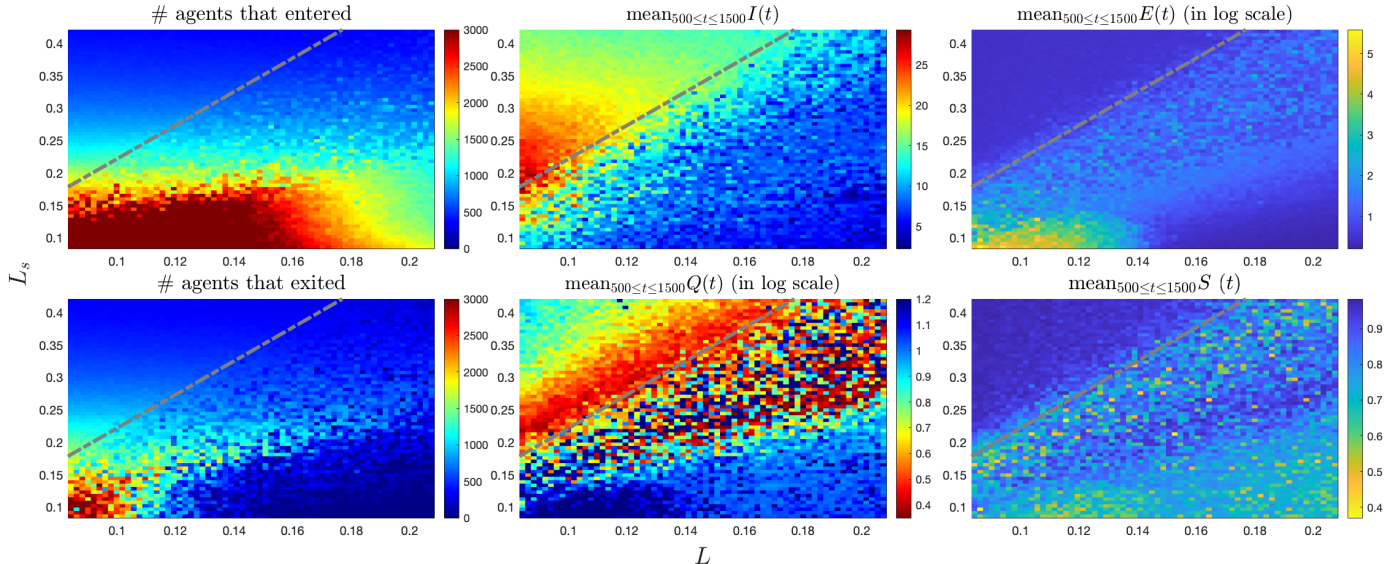


Figure 7: Phase diagram (L, L_s) for **Model I** on the bidirectional hallway under strong alignment $\nu = 2$ (with resolution of 65×65 points). The four observables from §5.1 are averaged over the time tail $t \in [500; 1500]$. The transition between steady unobstructed migrations and full obstruction of the hallway is quite blurry as opposed to its sharp counterpart for the case $\nu = 1$ shown in Figure 6. The region of steady unobstructed migration (i.e. small L and large L_s) that is qualitatively similar to its counterpart for $\nu = 1$ is found above the dashed gray line $L_s = 2.58L - 3.7 \times 10^{-2}$; there the data is robust under change in the random generator of the agent's entry. On the other hand, below the gray line the dynamics are rather unpredictable and showcase important vorticity.

domain $[0, l]^2$ and the 2-dimensional sphere. Here it is natural to define a dimensionless parameter $\mu > 0$ capturing the relative length scales based upon n , L , and $|\Omega|$. Roughly speaking μ should represent the ratio of the repulsive length scale to the average inter-agent distance. We take

$$\mu := \frac{L}{(|\Omega|/n)^{1/2}}.$$

Thus, on the torus $\mathbb{R}^2/l\mathbb{Z}^2$ of primary domain $[0, l]^2$, we have $\mu = L\sqrt{n/l^2} = \sqrt{n}L/l$ and on the sphere of radius R , we have $\mu = L\sqrt{n/(4\pi R^2)} = \sqrt{\frac{n}{\pi}} \frac{L}{2R}$.

6.1 Untargeted phase diagram

The μ - ν phase diagram is sketched in Figure 9. In the supplementary material we include simulations for these regimes as well as a brief description of their labels. We include as well simulations of all these regimes for the untargeted sphere (wherein a similar phase diagram is observed).

As in the case of the infinite plane (§4), the dynamics are simplified for lack of boundary interactions. We remark that in the absence of unbounded Voronoi cells, the dynamics of models I and II are not qualitatively different on compact domains and a lot of structure is preserved from one to the other. The governing equations are further simplified in case that no targets are assigned, we call such systems homing-free. Roughly speaking, the (μ, ν) phase space for homing-free systems on the torus and sphere are quite similar. Changes in μ and ν correlate

tightly with changes in clustering energy and polarization respectively. Here clustering energy is as described in the previous section. On the torus, polarization is as defined in the previous section with respect to the (arbitrary) coordinates inherited from $[0, l]^2$. For the sphere, by ‘‘polarization’’ we mean the angular momentum of the ensemble with respect to the (unit) sphere’s center viewing the position an orientation vectors as vectors in \mathbb{R}^3 in the natural way. In this section, we shall use the term ‘‘polarization’’ to talk about the sphere and torus at once. We find the following clearly distinct extremes.

Gaseous. (Small μ , small ν) When ν is small, orientations are spatiotemporally uncorrelated achieving polarization near zero. With small μ , agents only interact repulsively at distances small compared to the domain scale and so positions as well are essentially random and modest clustering energy persists (although no consistent clusters propagate noticeably through the agent medium).

Solid. (Large μ , small ν) As above, since ν is small, orientations remain uncorrelated and polarization near zero. But with large μ , mutual repulsion at lengths comparable to the domain scale force the system toward a uniformly spaced hexagonal crystalline structure (necessarily with defects due to the topological constraints) and extremely low clustering energy (near 1) is maintained. Furthermore, since the individual orientations are essentially random, the overall drift heading is near zero.

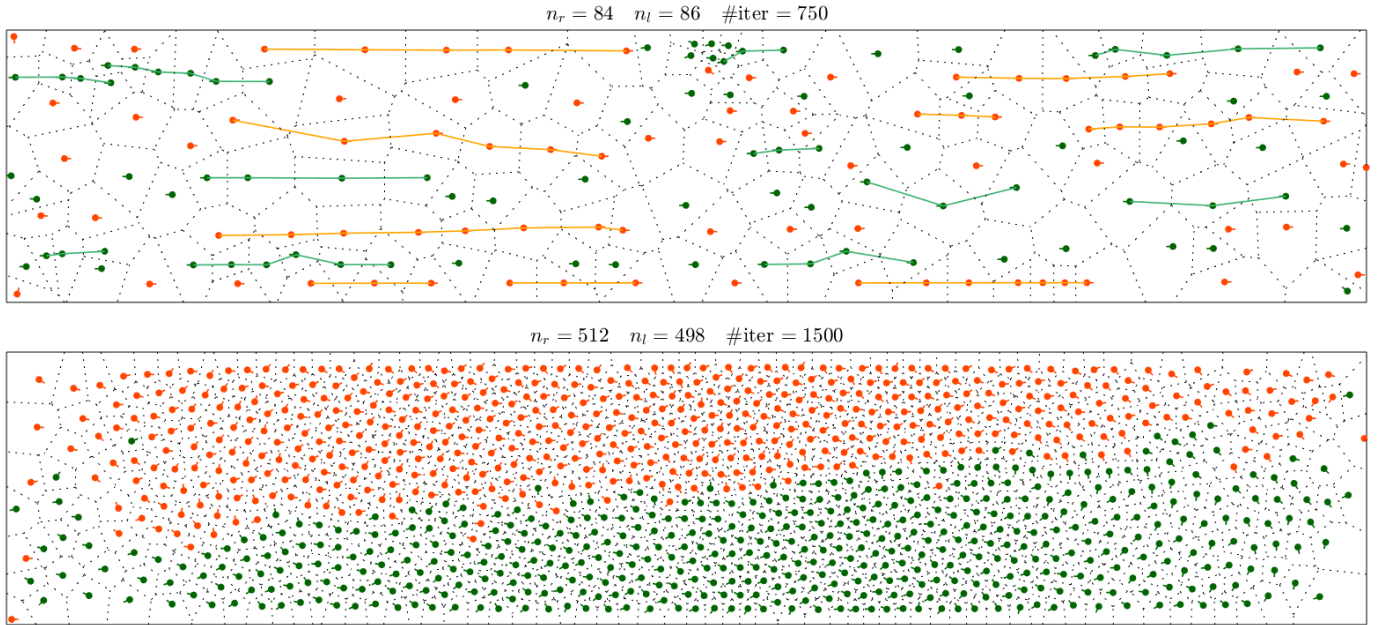


Figure 8: Emerging behaviors in the bidirectional corridor, agents X_r are shown in orange and X_l in green: (top) regime (II) shows significant amounts of queuing. The queuing structure (graph) \mathcal{Q}_r is displayed in orange and \mathcal{Q}_l in green. (bottom) regime (V) shows the two subpopulations separated by a long interface and “sliding” along each other.

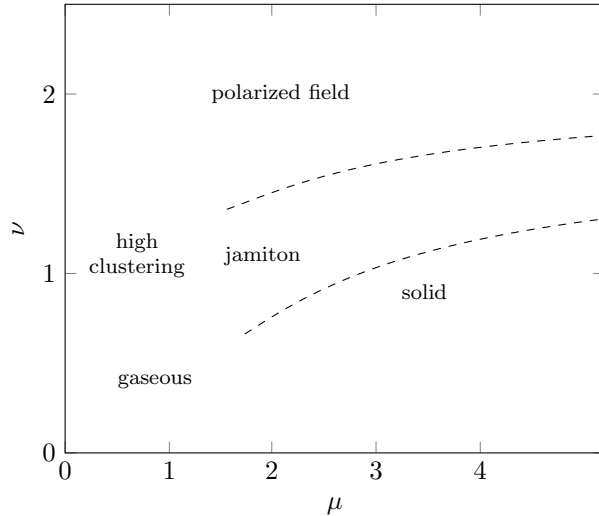


Figure 9: Untargeted phase diagram sketch with Model I for the torus. The dimensionless parameter μ is given by $\mu = L(n/|\Omega|)^{1/2} = \sqrt{n}L/l$. The dashed lines are merely conceptual delineations, not sharp bifurcation loci. Their rough shape is based on coarse probing of phase space with simulations. While the precise features of the phase diagram of course also depend on the particular choices of transition functions σ and g , the qualitative structure remains unchanged.

Flow. (Small μ , large ν) With large ν , the system quickly attains high polarization with near consensus in orientation. Again, for small μ , only modest clustering

energy persists with no clear structure in the agents’ positions.

Drift. (Large μ , large ν) Like the solid regime, large μ quickly drives the system to a near crystal structure but now also, neighbors tend to align their orientations and overall orientation consensus is attained (albeit slightly noisier than the flow regime due to significant nearest-neighbor interactions), thus achieving high polarization and an overall drift (with much less individual variation than the flow regime).

The transitional regimes are harder to characterize. For all values of μ , increasing through intermediate ν causes a gradual increase in polarization with no apparent bifurcations. Fixing ν and increasing through intermediate μ also does not show sharp bifurcations but at intermediate values of μ and moderate or large ν , one observes one or several (depending on the number of agents) persistent clusters which propagate backward (against the drift heading) through the agent medium, akin to what has been observed in traffic flow. Indeed, for sufficiently few agents (a few hundred), at intermediate μ and ν , one finds a single large patch of more densely packed agents with less correlated orientation propagating backward against a comparably large patch of sparser (hence faster) agents with near consensus in orientation.

6.2 Point targets

We further include simulations on the torus and the sphere for one, two and three point targets (wherein all

agents always seek their nearest target point). The emergent dynamics are complicated, even for such simple target configurations. Nonetheless, we remark qualitatively.

In all cases, the behavior for very strong alignment is essentially similar to the homing free case (Section §6.1), achieving near orientation consensus with only slight deviation close to the target points. Compare this with the single-point target behavior in the (non-compact) planar case of Section §4, where the target has manifest influence for extremely strong alignment. This can be understood as a size effect of the compact domains. Whereas, in the strong alignment single-point target planar case, ensembles of agents may adopt wide orbits about the target point because (i) agents may always in principle spread out enough that homing dominates the homing-repulsion effect, giving each agent’s steps a radial component with respect to the target and (ii) there exist wide enough orbits in the plane that this radial component—feeble against the magnitude $\approx \nu$ alignment component—is sufficient. Clearly these are not both possible on compact domains, any minimum average distance between agents imposes a minimum path length for a size n ensemble, and sufficiently long paths in compact domains will interfere with themselves (to within the ensemble density).

For sufficiently weak alignment with a single point target, the behavior is much like in the planar case. Although this is what one would expect, it is not entirely trivial. Namely, alignment, as we have formulated it, exerts direct influence on neighboring agents and on these domains, a pinwheel or ring system has a rather different Delaunay topology than the analogous planar systems, with agents near opposite edges of the ensemble will neighbor each other.

For two and three point targets, we encourage readers to explore the simulations and we comment only on the following curiosity. In the torus, we (mostly arbitrarily) considered two target points placed bisecting a minimal (closed) geodesic. In most of the parameter space (again for sufficiently weak alignment), the system robustly organizes into a “cog” behavior, with counter-rotating ensembles surrounding the two target points. The analogous setup in the plane yields like behavior for appropriate parameter values. However, in a certain parameter range, the torus exhibited a behavior, which we call the “anti-cog”, whereby the system would settle into two co-rotating ensembles about the target points, with some continual agent exchange between them. This anti-cog behavior could not be reliably reproduced on the plane. On compact domains, emergence of the anti-cog behavior was sensitive to initial conditions in the sense that, in this parameter range, for uniformly sampled position/orientation initial conditions, the system would either settle into the cog or anti-cog behavior. More specifically, we found two sub regimes in the (μ, ν) phase plane, one in which the cog behavior was by far dominant amongst random initializations and one in which the anti-cog emerged for a substantial fraction of initial-

izations. Whether the emergence of the anti-cog behavior is a size effect or a topological one or both is unclear.

7 Advancing the scope of VTP

With minimal modifications the model can be applied to an extremely broad class of situations. With no modification whatsoever, the model as presented here allows for (1) any convex domain with or without boundary and (2) arbitrarily many distinct classes of agents seeking distinct targets (each of which can be any subset of the domain). With minimal modification, our model can be made to (3) include sources and sinks of agents and (4) support non-convex domains so as to include obstacles in the environment.

In order to use VTP for environments with impassable obstacles like interior walls, pillars, et cetera, we must implement the model for non-convex domains. Such environmental obstacles can be viewed as “holes” or “inlets” in the domain. As suggested in Section 3, the necessary modification to the model for such domains has to do with the Euclidean distance. A metric can be defined which is consistent with our cognitive assumptions for agents and whose Voronoi diagram remains the natural fundamental structure upon which to construct VTP. While the modification is simple and natural, it does present certain computational difficulties in running simulations and this is the subject of current work. This raises the broader issue of constructing different metrics with which to build the Voronoi diagram. Voronoi diagrams in arbitrary metrics are much less well understood and computational methods involving them are lacking. Nonetheless, the question of determining the “right” metric for a given setup under VTP is intriguing.

Three other possible generalizations are as follows: (1) the alignment a_i of a population with higher situational awareness can be computed over “neighbors” $j \sim \leq^m i$ within a larger (Delaunay) topological radius for $m \geq 1$, i.e., over all agents whose (path-wise) distance to i in $DT(X)$ is at most m . This can be implemented without significant increase in computational complexity as one needs only compute powers of the already obtained $DT(X)$ adjacency matrix. Moreover, this property need not be the same among all agents. Indeed one might introduce variety among the agents both with respect to alignment and repulsion. (2) Limited vision of the targets T_i can be modelled within the topological framework by enforcing $h_i \neq 0$ only if $T_i \cap \bigcup_{j \sim \leq^s i} V_j \neq \emptyset$ for some specified integer s . We remark that the notion of m -topological radii naturally allows integration of a component of attraction for aggregation in a more classical zone-based context. Specifically, alignment and attraction can act over concentric “layers” $j \sim \leq^{m_1} i$ and $j \sim \leq^{m_2} i$ but $j \not\sim \leq^{m_1} i$ respectively with $1 \leq m_1 < m_2$. (3) The original VTP as well as its possible extensions can be brought to heterogeneous crowds where agents act and

respond differently to stimuli. An important example is when only a fraction of “active” agents are mindful of their targets; very much like the effective leadership analysis performed in [10], the amount of target-knowledge transferred to “passive” agents can be studied to test the relevance of the VTP framework in the context of panic crowd dynamics. It is highly likely here that one needs to incorporate into VTP some form of agent attraction at “large” distances.

References

- [1] Shin Mi Ahn, Heesun Choi, Seung-Yeal Ha, and Ho Lee. On collision-avoiding initial configurations to cucker-smale type flocking models. *Communications in Mathematical Sciences*, 10(2):625–643, 2012.
- [2] L. Atia, D. Bi, Y. Sharma, J.A. Mitchel, B. Gweon, S.A. Koehler, S.J. DeCamp, B. Lan, J.H. Kim, R. Hirsch, A.F. Pegoraro, K.H. Lee, J.R. Starr, D.A. Weitz, A.C. Martin, J.A. Park, J.P. Butler, and J.J. Fredberg. Geometric constraints during epithelial jamming. *Nature Physics*, 14(6):613–620, apr 2018.
- [3] Franz Aurenhammer, Rolf Klein, and Der-Tsai Lee. *Voronoi diagrams and Delaunay triangulations*. World Scientific Publishing Company, 2013.
- [4] M. Ballerini, N. Cabibbo, R. Candelier, A. Cavagna, E. Cisbani, I. Giardina, V. Lecomte, A. Orlandi, G. Parisi, A. Procaccini, M. Viale, and V. Zdravkovic. Interaction ruling animal collective behavior depends on topological rather than metric distance: Evidence from a field study. *Proceedings of the National Academy of Sciences*, 105(4):1232–1237, 2008.
- [5] Sara Bernardi and Marco Scianna. An agent-based approach for modelling collective dynamics in animal groups distinguishing individual speed and orientation. *Philosophical Transactions of the Royal Society B: Biological Sciences*, 375(1807):20190383, jul 2020.
- [6] Andrew J Bernoff and Chad M Topaz. A primer of swarm equilibria. *SIAM Journal on Applied Dynamical Systems*, 10(1):212–250, 2011.
- [7] D. Bi, J.H. Lopez, J.M. Schwarz, and M.L. Manning. A density-independent rigidity transition in biological tissues. *Nature Physics*, 11(12):1074–1079, sep 2015.
- [8] Yuxin Chen and Theodore Kolokolnikov. A minimal model of predator–swarm interactions. *Journal of The Royal Society Interface*, 11(94):20131208, 2014.
- [9] Young-Pil Choi, Seung-Yeal Ha, and Zhuchun Li. *Emergent dynamics of the Cucker-Smale flocking model and its variants*, pages 299–331. Springer International Publishing, Cham, 2017.
- [10] Iain D Couzin, Jens Krause, Nigel R Franks, and Simon A Levin. Effective leadership and decision-making in animal groups on the move. *Nature*, 433(7025):513–516, 2005.
- [11] Iain D Couzin, Jens Krause, Richard James, Graeme D Ruxton, and Nigel R Franks. Collective memory and spatial sorting in animal groups. *Journal of theoretical biology*, 218(1):1–11, 2002.
- [12] F. Cucker and S. Smale. Emergent behavior in flocks. *IEEE Transactions on Automatic Control*, 52(5):852–862, May 2007.
- [13] Felipe Cucker and Jiu-Gang Dong. Avoiding collisions in flocks. *IEEE Transactions on Automatic Control*, 55(5):1238–1243, 2010.
- [14] Maria R D’Orsogna, Yao-Li Chuang, Andrea L Bertozzi, and Lincoln S Chayes. Self-propelled particles with soft-core interactions: patterns, stability, and collapse. *Physical review letters*, 96(10):104302, 2006.
- [15] Qiang Du, Vance Faber, and Max Gunzburger. Centroidal voronoi tessellations: Applications and algorithms. *SIAM review*, 41(4):637–676, 1999.
- [16] Leah Edelstein-Keshet, James Watmough, and Daniel Grunbaum. Do travelling band solutions describe cohesive swarms? an investigation for migratory locusts. *Journal of mathematical biology*, 36(6):515–549, 1998.
- [17] Radek Erban, Jan Haskovec, and Yongzheng Sun. A cucker–smale model with noise and delay. *SIAM Journal on Applied Mathematics*, 76(4):1535–1557, 2016.
- [18] F. Ginelli and H. Chate. Relevance of metric-free interactions in flocking phenomena. *Physical Review Letters*, 105(16), oct 2010.
- [19] Ivan Gonzalez, Rustum Choksi, and Jean-Christophe Nave. A simple geometric method for navigating the energy landscape of centroidal voronoi tessellations. *SIAM Journal on Scientific Computing*, 43(2):A1527–A1554, 2021.
- [20] Guillaume Grégoire and Hugues Chaté. Onset of collective and cohesive motion. *Phys. Rev. Lett.*, 92:025702, Jan 2004.
- [21] Guillaume Grégoire, Hugues Chaté, and Yuhai Tu. Active and passive particles: Modeling beads in a bacterial bath. *Physical Review E*, 64(1):011902, 2001.
- [22] Guillaume Grégoire, Hugues Chaté, and Yuhai Tu. Moving and staying together without a leader. *Physica D: Nonlinear Phenomena*, 181(3):157–170, 2003.

- [23] Dirk Helbing. Traffic and related self-driven many-particle systems. *Reviews of Modern Physics*, 73, 12 2000.
- [24] Dirk Helbing, Illes Farkas, and Tamas Vicsek. Freezing by heating in a driven mesoscopic system. *Physical review letters*, 84(6):1240, 2000.
- [25] Dirk Helbing and Péter Molnár. Social force model for pedestrian dynamics. *Physical Review E*, 51(5):4282–4286, may 1995.
- [26] Christos C Ioannou, Vishwesha Guttal, and Iain D Couzin. Predatory fish select for coordinated collective motion in virtual prey. *Science*, 337(6099):1212–1215, 2012.
- [27] Ali Jadbabaie, Jie Lin, and A Stephen Morse. Coordination of groups of mobile autonomous agents using nearest neighbor rules. *IEEE Transactions on automatic control*, 48(6):988–1001, 2003.
- [28] S-H Lee, HK Pak, and T-S Chon. Dynamics of prey-flock escaping behavior in response to predator’s attack. *Journal of theoretical biology*, 240(2):250–259, 2006.
- [29] Naomi Ehrich Leonard and Edward Fiorelli. Virtual leaders, artificial potentials and coordinated control of groups. In *Proceedings of the 40th IEEE conference on decision and control (Cat. No. 01CH37228)*, volume 3, pages 2968–2973. IEEE, 2001.
- [30] Herbert Levine, Wouter-Jan Rappel, and Inon Cohen. Self-organization in systems of self-propelled particles. *Physical review. E, Statistical, nonlinear, and soft matter physics*, 63:017101, 02 2001.
- [31] Magnus Lindhe, Petter Ogren, and Karl H. Johansson. Flocking with obstacle avoidance: a new distributed coordination algorithm based on voronoi partitions. In *Proceedings of the 2005 IEEE International Conference on Robotics and Automation*. IEEE, 2005.
- [32] Yicheng Liu and Jianhong Wu. Flocking and asymptotic velocity of the cucker-smale model with processing delay. *Journal of Mathematical Analysis and Applications*, 415(1):53–61, 2014.
- [33] Alex Mogilner, Leah Edelstein-Keshet, L. Bent, and A. Spiros. Mutual interactions, potentials, and individual distance in a social aggregation. *Journal of mathematical biology*, 47:353–389, 2003.
- [34] Alexander Mogilner and Leah Edelstein-Keshet. A non-local model for a swarm. *Journal of mathematical biology*, 38(6):534–570, 1999.
- [35] Siddhant Mohapatra and Pallab Sinha Mahapatra. Confined system analysis of a predator-prey minimalist model. *Scientific Reports*, 9(1), aug 2019.
- [36] Sébastien Motsch and Eitan Tadmor. A new model for self-organized dynamics and its flocking behavior. *Journal of Statistical Physics*, 144(5):923–947, aug 2011.
- [37] Atsuyuki Okabe and David George Kendall. *Spatial tessellations concepts and applications of Voronoi diagrams*. John Wiley & Sons, Chichester; New York, 2000.
- [38] R. Olfati-Saber. Flocking for multi-agent dynamic systems: Algorithms and theory. *IEEE Trans. on Automatic Control*, 51(3):401–420, mar 2006.
- [39] R. Olfati-Saber, J.A. Fax, and R.M. Murray. Consensus and cooperation in networked multi-agent systems. *Proceedings of the IEEE*, 95(1):215–233, jan 2007.
- [40] R. Olfati-Saber and R.M. Murray. Consensus problems in networks of agents with switching topology and time-delays. *IEEE Trans. on Automatic Control*, 49(9):1520–1533, sep 2004.
- [41] Jaemann Park, H Jin Kim, and Seung-Yeal Ha. Cucker-smale flocking with inter-particle bonding forces. *IEEE Transactions on Automatic Control*, 55(11):2617–2623, 2010.
- [42] Craig W. Reynolds. Flocks, herds and schools: A distributed behavioral model. *ACM SIGGRAPH Computer Graphics*, 21(4):25–34, aug 1987.
- [43] Jackie Shen. Cucker-smale flocking under hierarchical leadership. *SIAM Journal of Applied Mathematics*, 68:694–719, 01 2007.
- [44] A. Strandburg-Peshkin, C.R. Twomey, N. Bode, A.B. Kao, Y. Katz, C.C. Ioannou, S.B. Rosenthal, C.J. Torney, H.S. Wu, S.A. Levin, and I.D.]Cousin. Visual sensory networks and effective information transfer in animal groups. *23(17):R709–R711*, sep 2013.
- [45] Chad M Topaz, Andrew J Bernoff, Sheldon Logan, and Wyatt Toolson. A model for rolling swarms of locusts. *The European Physical Journal Special Topics*, 157(1):93–109, 2008.
- [46] Tamás Vicsek, András Czirók, Eshel Ben-Jacob, Inon Cohen, and Ofer Shochet. Novel type of phase transition in a system of self-driven particles. *Phys Rev Lett*, 75:1226–1229, Aug 1995.
- [47] Yao Xiao, Ziyou Gao, Yunchao Qu, and Xingang Li. A pedestrian flow model considering the impact of local density: voronoi diagram based heuristics approach. *Transportation research part C: emerging technologies*, 68:566–580, 2016.

- [48] Jun Zhang, Wolfram Klingsch, Andreas Schadschneider, and Armin Seyfried. Ordering in bidirectional pedestrian flows and its influence on the fundamental diagram. *Journal of Statistical Mechanics: Theory and Experiment*, 2012(02):P02002, 2012.